Rayleigh-Bénard convection in the presence of a radial ramp of the Rayleigh number

Kapil M. S. Bajaj, Nathalie Mukolobwiez, Jaechul Oh, and Guenter Ahlers

Department of Physics and iQCD, University of California, Santa Barbara, California 93106, USA

Abstract. We present experimental results for pattern formation in a thin horizontal fluid layer heated from below. The fluid was SF_6 at a pressure of 20.0 bars with a Prandtl number of 0.87. The cylindrical sample had an interior section of uniform spacing $d = d_0$ for radii $r < r_0$ and a ramp $d(r)$ for $r > r_0$. For Rayleigh numbers $R_0 > R_c$ in the interior, straight or slightly curved rolls with an average wave number $\langle k_s \rangle = \tilde{k}_c + k_1 \varepsilon_0$ ($\varepsilon_0 \equiv R_0/R_c - 1$) with $k_1 \simeq 0.8$ were selected. The critical wave number $\tilde{k}_c$ depended sensitively on the cell spacing. For the largest $\tilde{k}_c$ the patterns were skewed-varicose unstable and dislocation pairs were generated repeatedly in the interior and for all ε. For slightly smaller $\tilde{k}_c$ time-independent rolls were stable for $\varepsilon \lesssim 0.15$, but for larger ε the skewed-varicose instability was encountered near the sample center and dislocation pairs were formed repeatedly for all samples. When stationary rolls were stable, their slight curvature and the width of their wave-number distribution slowly increased with ε. This led to a complicated shape and overall broadening of the structure factor $S(k)$. For $\varepsilon \lesssim 0.05$ the inverse width ξ_2 of $S(k)$ was roughly constant and presumably limited by the finite sample size, but for larger ε we found $\xi_2 \propto \varepsilon^{-0.5}$.

Key words: Hydrodynamic instabilities, Patterns

1. Introduction

Convection of a thin horizontal layer of fluid heated from below (Rayleigh-Bénard convection, RBC) occurs when the temperature difference ΔT exceeds a critical value ΔT_c. [1] It offers opportunities for the experimental study of numerous pattern-formation phenomena. [2, 3] In the absence of significant thermal-noise-induced fluctuations [4, 5, 6] the bifurcation is predicted to be supercritical, i.e. the amplitude of the convection is expected to increases continuously from zero as ΔT increases beyond ΔT_c. [7] For a layer of infinite lateral extent the pattern above but close to onset is predicted to consist of straight rolls. [7] In the finite samples used in laboratory experiments the bifurcation remains supercritical, but usually the side wall of the sample induces deviations from the anticipated perfect parallel-roll pattern in the form of domain walls, roll curvature, wall foci, dislocations, and concave disclinations as illustrated in Fig. 1. [8, 9, 10]

In the present work we made an effort to reduce, change, or eliminate the influence of the side wall on the pattern. We did this by using a sample cell with a central uniform section of aspect ratio $\Gamma_0 \simeq 40$ and a radial ramp in the cell spacing [11] for larger radii. In this geometry convection started in the uniform section, and the pattern spread radially towards the side wall only as $\varepsilon \equiv \Delta T/\Delta T_c - 1$ increased beyond zero. Thus, for $\varepsilon \lesssim 0.25$ the convection amplitude decreased gradually and finally vanished with increasing radius while there was only quiescent fluid adjacent to the wall. Under these conditions no defects or roll curvature could be generated at the wall.

It turns out that the ramp in the cell spacing exerts other subtle influences on the pattern. [11, 12] The effect of a spatial ramp of the control parameter on the pattern-formation process was a topic of great interest a couple of decades ago [2, 13, 14, 15, 16, 17, 18, 19, 20, 21, 22, 23, 24]. It was studied primarily for one-dimensional systems such as Taylor-vortex flow [14, 17, 20, 23, 24], Rayleigh-Bénard convection in narrow channels [22], and certain mathematical models [15]. The reason for the interest was that one of the major issues in pattern formation is how a given system selects a particular wave number out of a continuous band of stable states. This selection problem had been studied only for a small number of specific cases [2]. The spatial ramp can provide such a mechanism. For the idealized case where the ramp has a vanishing slope but nonetheless extends from below to above onset, one expects that the selected wave number k_s at the point where $\varepsilon = 0$ is equal to the critical wave number k_c. This is predicted to be sufficient to fix k_s everywhere along the ramp and in the homogeneous interior. It is expected to lead to a time independent pattern near onset. For small ε, k_s in the interior should then be given by

$$k_s = \tilde{k}_c + k_1\varepsilon \tag{1}$$

with $\tilde{k}_c = k_c$ and k_1 dependent on the nature of the ramp and, in the case of RBC, on the Prandtl number $\sigma \equiv \nu/\kappa$ (ν is the kinematic viscosity and κ is the thermal diffusivity).

In the physical system the ramp angle is finite. Even below onset this usually leads to a large-scale flow (LSF) [25, 26] with a characteristic length scale much larger than a

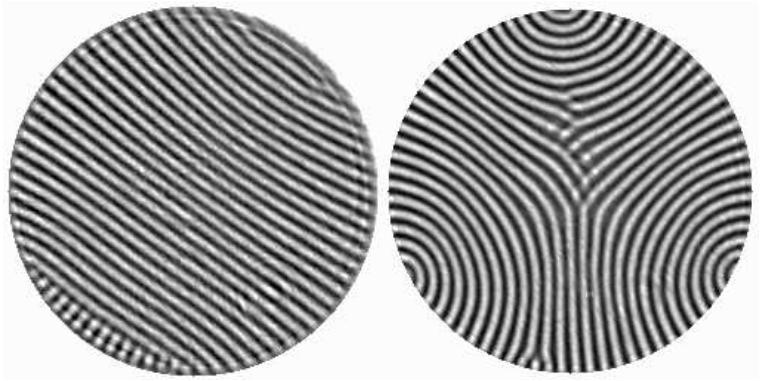

Figure 1. Shadow-graph images of convection patterns in a sample of aspect ratio $\Gamma = 30$ with a rigid side wall. The sample was Argon at a mean temperature of 23.45 °C and a pressure of 29.7 bars where the Prandtl number is $\sigma = 0.69$. Left: $\varepsilon = 0.07$. Right: $\varepsilon = 0.20$. Adapted from Ref. [10].

roll wavelength which interacts with and modifies the roll structure in the interior and above R_c. For our geometry (see Sect. 2.1) one would expect this flow to be in the radial direction, and to be directed outward near the bottom and inward near the top of the cell, so that the vertical average of the horizontal velocity vanishes. Recently this was confirmed by direct numerical simulations (DNS) using the Boussinesq equations of motion for a RBC system with a radial ramp similar to ours but with smaller aspect ratios $\Gamma_0 \leq 20$. [12] The DNS also revealed that, in addition to the LSF, there is a mean flow (MF) which has a non-vanishing vertical average of the horizontal velocity field and which is induced by the roll-amplitude variation in the ramped region. [12] The MF had a quadrupolar structure and induced weak roll curvature. Interesting but complicated structures of the roll wave-number were observed experimentally [11] in this system which presumably were due to interactions between the LSF and MF and the convection rolls. In the one-dimensional cases which were studied in the past this interaction is somewhat simpler and understood in more detail. In that case there is a LSF but no MF. For a finite ramp angle one then obtains a wave number which is selected out of a narrow band and which depends periodically on the aspect ratio [20, 21, 24, 27]. This is so because the finite ramp angle tends to pin the phase of the structure and thus tends to select wavelengths which are commensurate with the length of the uniform section. In this case the bifurcation is rendered imperfect and the wave number may differ from k_c even in the vicinity of onset for the perfect system.

The major features of results for the pattern selection due to the radial ramp for one particular sample (sample 2 in Table 1) were presented before [11]. In the present paper we provide more detailed experimental results for measurements using several different samples. We found that the ramp did indeed select a wave number that varied linearly with ε, with a slope $k_1 \simeq 0.8$. This feature agrees well with the DNS. [12] However, the wave number at onset $\tilde{k}_c$, although well defined for a given experimental sample, was not reproducible when the sample spacing was changed by only a small

Table 1. Parameters for the experimental samples. The uncertainty of ΔT_c is approximately 0.002°C. Entries marked by * correspond to unstable states.

Sample	ΔT_c (°C)	d_0 (cm)	Γ_0	$\tilde{k}_c$	k_1
1	1.774	0.0585	54.3	3.086	0.81
2	0.8287	0.0752	42.3	2.952	0.94
3	0.8215	0.0755	42.1	3.007	0.79
4	0.8382	0.0750	42.4	2.985	0.83
5	0.5495	0.0864	36.8	$\gtrsim 3.1^*$	$\simeq 0.8^*$

amount. Generally it did not coincide with k_c. This aspect of the experiment does not agree with the results obtained from DNS, and we do not have an explanation for it. In all but one of the experimental samples the pattern near onset was time independent. However, in those cases time dependence occurred when ε exceeded about 0.15. In that parameter range the wave number near the sample center had exceeded the skewed-varicose instability boundary of the laterally infinite straight-roll pattern, and dislocation pairs formed repeatedly near the sample center. In one case (sample 5), the value of $\tilde{k}_c$ was exceptionally large and the pattern above onset was found to be skewed-varicose unstable at all ε.

In Sect. 2.1 we describe our apparatus, sample cell, and experimental procedure in detail. We discuss our image-analysis methods in Sect. 2.2. In Sect. 3 we present our results, and a brief summary is given in Sect. 4.

2. Apparatus, Experimental Procedure, and Image Analysis

2.1. The apparatus and procedure

Measurements were made in apparatus similar to that described in detail elsewhere [28]. The fluid was sulfur hexafluoride (SF_6) at a pressure of 20.04 bar and a fixed mean temperature of 38.00°C. Two distinct cells were used. Their top plates were optically flat sapphires. The bottoms were diamond-machined aluminum plates. The top surfaces of the bottom plates had plane central sections of radii $r_0 = 3.18$ cm. In these sections the uniform cell spacings were determined interferometrically [28] at the beginning of the experiments with sample 1 and 2 to be $\tilde{d}_0 = 590 \pm 2\mu$m and $760 \pm 2\mu$m respectively. At various times, the bottom-plate alignment was re-adjusted with three externally-accessible setscrews [28] so as to minimize the spatial variation of d_0. This adjustment had the potential to change the average value of d_0 by a few μm. At other times we deliberately used these setscrews to change d_0 to examine the effect on the wave-number selection. Starting with sample 2, this led to the remaining samples. In order to have consistent values of d_0 throughout these measurements, we used the onset of convection together with the fluid properties [29] to determine d_0 after each such adjustment. Those values of d_0 are listed in Table 1. Also given in that table are the

aspect ratios $\Gamma_0 = r_0/d_0$ of the uniform central section of the cell. We refer to each of the cell spacings as different samples. Sample 2 was used to obtain the data of Ref. [11].

Over the radius range $r_0 < r < r_1 = 4.44$ cm the bottom plate had a profile which yielded

$$\frac{d}{d_0} = 1 - \delta \left[1 - cos \left(\frac{(r - r_0)\pi}{r_1 - r_0} \right) \right] \quad . \tag{2}$$

The values of δ differed slightly for different samples because d_0 differed. They correspond to a total rise of the ramp between r_0 and r_1 of 53 μm. Since $R \propto d^3$, $R/R_0 \propto (d/d_0)^3$. A paper side wall was located immediately beyond r_1 but played at most a minor role since the pattern never reached it.

We used shadowgraph visualization [28] for $0 < r \lesssim r_0$. For larger r the bottom-plate profile deflected the shadowgraph beam and no image was formed. The distance Δx between pixels was $233 \pm 1\mu$m. Overall systematic errors of $\Delta x/d_0$, and thus of q, were no larger than 1.5% corresponding to $\delta q \simeq \pm 0.045$.

The radial-ramp geometries assured that convection started first in the central sections when ΔT reached a critical value ΔT_c. At modest values of $\varepsilon \equiv \Delta T/\Delta T_c - 1 > 0$ the convection rolls extended some distance into the ramped regions, but instead of reaching a side wall, their amplitude smoothly vanished with increasing radius. We estimate that the location of vanishing convection-amplitude remained in the ramped region for ε up to 0.41 for sample 1 and up to 0.22 for the other samples. Thus, over this ε-range the conventional effect of a side wall on the pattern was eliminated, although the ramp induced its own interesting effects on the pattern formation [11].

For radii $r < r_0$ we determined the variation of the cell spacings with an expanded He-Ne laser beam. Since the bottom plates were not quite optically flat, there remained about three nearly-circular approximately-concentric interference rings when the cell was illuminated from above. For sample 3 for instance this implied a radial variation of the cell spacing by about one μm or 0.13 %. Since the Rayleigh number depends on d_0^3, this implies that the onset of convection in the central section of cell II should occur over an ε-interval of about 0.004. Thus we cannot expect to make meaningfull measurements at even smaller ε.

The top- and bottom-plate temperatures were held constant. Their typical standard deviations from a fixed temperature were about 0.2 mK. The pressure was regulated using a "hot volume" technique. This method consisted of regulating the temperature of a gas volume external to but connected with the main apparatus in a feedback loop under control of a pressure gage. The standard deviation of the pressure from its set point typically was 2×10^{-4} bars. The shift of ΔT_c due to such a pressure fluctuation is only about 3×10^{-5}°C, i.e. negligible.

Based on the fluid properties [29] and the spacing, the vertical thermal diffusion time was $\tau_v \equiv d^2/\kappa \simeq 2.5$ sec for sample 1 and 4.2 sec for samples 2 to 4. The Prandtl number was $\sigma \equiv \nu/\kappa = 0.867$. The samples conformed extremely well to the Boussinesq approximation. At onset, the parameter Q introduced by Busse [30] which describes

the deviations from this approximation had the value 0.30 for sample 1 and 0.135 for the others. The parameters for all the runs are given in Table 1.

The convection patterns were determined with the shadowgraph method [28]. The shadowgraph contrast was used also to determine ΔT_c.

2.2. Image Analysis

At each ΔT, a sequence of typically 64 or 128 shadowgraph images was acquired. The time interval δt between them was typically 15 s. For a suitable ΔT close to but below ΔT_c a sequence was averaged to provide a background image $\tilde{I}_o(\mathbf{x})$. Here $\mathbf{x}$ is the horizontal position vector. Averaging was used only for the background; all images for positive ε were analyzed individually. The images were corrected to the true black level by a constant additive correction of the framegrabber output, and then all images $\tilde{I}_i(\mathbf{x})$ of the experimental run were divided by $\tilde{I}_o(\mathbf{x})$ to yield the signal images

$$I_i(\mathbf{x}) \equiv [\tilde{I}_i(\mathbf{x}) - \tilde{I}_o(\mathbf{x})]/\tilde{I}_o(\mathbf{x}) \quad . \tag{3}$$

The mean of $I_i(\mathbf{x})$ typically was within ± 0.01, indicating adequate stability of the light intensity and image-acquisition system. The deviation from the mean is the desired signal plus the experimental noise. At our largest ε its mean-square value (equal to the total power of the Fourier transform) approached 0.04. Fourier analysis did not reveal any second-harmanic contribution to the patterns, suggesting that the shadowgraph operated in the weak-diffraction limit [31, 32]. For pattern visualization $I_i(\mathbf{x})$ was usually re-scaled using its own variance to determine the grey levels. However, for further image analysis, the unscaled signal images were used. The Fourier transform (FT) was obtained, and the structure factor (the square $S(\mathbf{k})$ of the modulus $F(\mathbf{k})$ of the FT) was used for further analysis. In the second and third row of Fig. 2 $F(\mathbf{k})$ corresponding to the images in the first row are shown. We usually applied a radial band-pass filter, centered around the peak of $S(\mathbf{k})$, in order to reduce experimental noise. Often this filtered FT was back-transformed to yield a real-space image less encumbered by experimental noise.

We sometimes used the azimuthal average $S(k) = \langle S(k,\theta)\rangle_\theta$ for further analysis. The total power

$$P = 2\pi \int_0^\infty kS(k)dk \tag{4}$$

is equal to the variance of $I_i(\mathbf{x})$ by Parseval's theorem. We used it to determine the onset of convection at ΔT_c. We calculated mean wave numbers

$$\langle k_s \rangle \equiv \frac{\int_0^\infty k^2 S(k)dk}{\int_0^\infty kS(k)dk} \ . \tag{5}$$

A two-point correlation length was obtained from

$$\xi_2^{-1} \equiv \left[\frac{\int_0^\infty (k-\langle k\rangle)^2 kS(k)dk}{\int_0^\infty kS(k)dk}\right]^{1/2} \ . \tag{6}$$

Because of the complicated shape of $S(\mathbf{k})$ these integrals were determined numerically by summing over points in Fourier space.

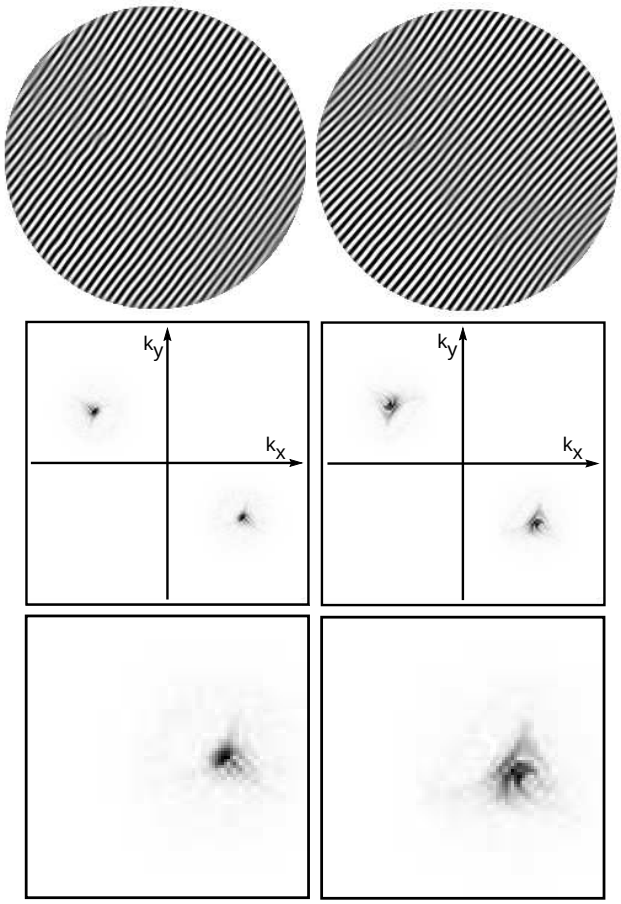

Figure 2. Images and Fourier-transform moduli from sample 3. Left column: $\varepsilon = 0.05$. Right column: $\varepsilon = 0.15$. First row: real-space images. Here the entire uniform section of the cell is shown. An mpeg movie for $\epsilon = 0.15$ can be found at Fig2-right.mpeg. At 30 frames/sec it is running at 112.5 times real speed. It covers a real-time interval of about 16 minutes and shows that the pattern is stationary. Second row: Moduli of the Fourier transforms. The k_x- and k_y-axes extend from -4.73 to +4.73. Third row: closeup view of part of the lower-right quadrant of the middle row. Now the origin is in the upper left corner, and $0 < k_x < 3.55$ and $0 > k_y > -3.55$.

3. Results

Early results were obtained with sample 2 and were reported before [11]. Here we provide some additional information, and results for some other runs.

The top row of Fig. 2 shows typical patterns for $\varepsilon = 0.05$ and 0.15. A movie from this run, at 450 times physical speed, can be found at Fig2-right.mpeg. It shows that the pattern is stationary. It turns out that the wave-number distributions in physical space of these seemingly perfect parallel straight rolls contain significant structure. This was discussed in detail before [11]. Here we show the modulus of the Fourier transform $F(\mathbf{k})$ in the middle row of the figure, with a closeup of one of the peaks in the bottom row. One sees that the structure in real space manifests itself in the form of side bands

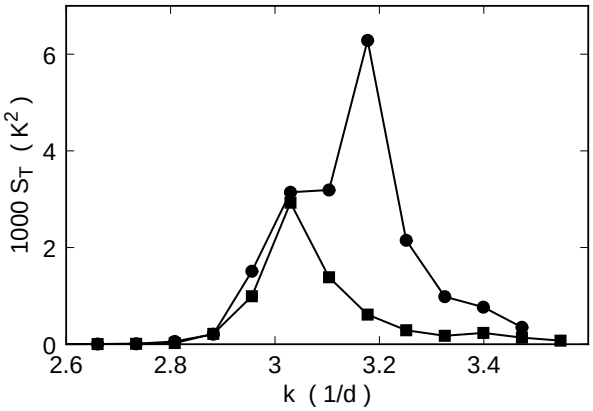

Figure 3. The temperature structure-factor $S_T(k)$ as a function of k for $\varepsilon = 0.05$ (squares) and $\varepsilon = 0.15$ (circles) for $\Omega = 0$ and from sample 3.

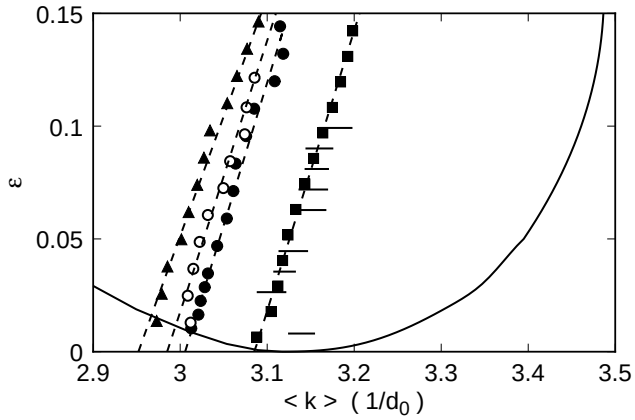

Figure 4. The mean wave number $\langle k \rangle$ at various ε and for several samples. Solid squares: sample 1. Solid triangles: sample 2. Solid circles: sample 3. Open circles: sample 4. Solid horizontal bars: the range of $\langle k \rangle$ covered during the repeated formation of dislocations pairs in the interior of sample 5. The solid curve is the theoretical stability boundary of infinitely extended straight rolls. The dashed lines are straight-line fits to the data. Their parameters are given in Table 1.

in Fourier space.

Figure 3 shows $S_T(k)$, i.e. the azimuthal average of $S_T(\mathbf{k})$. The structure revealed in Fig. 2 yields an asymmetric shape for $S_T(k)$ which is not readily fitted by any simple function. Thus the moments were computed using discrete sums over the actual data points. This process was relatively unencumbered by experimental noise because the noise could be filtered out over much of Fourier space. The results were not very sensitive to the range of k used for this summation.

In Fig. 4 we show the mean wave numbers at various ε which were obtained from several samples. As expected, the data fall on straight lines and can be described by Eq. 1. The slopes k_1 of the lines are nearly the same for all samples, but the wave number $\tilde{k}_c$ at onset varies from sample to sample. Both $\tilde{k}_c$ and k_1 are listed in Table 1.

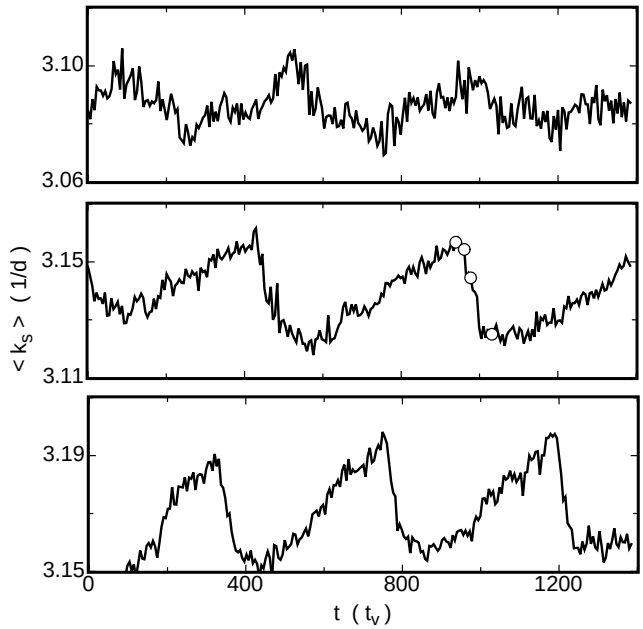

Figure 5. The mean wave number $\langle k_s \rangle$ for sample 5 as a function of the time t for (from top to bottom) $\varepsilon = 0.015$, 0.054, and 0.099. The open circles in the middle section correspond to the images shown in Fig. 6

One possible explanation for the variation of $\tilde{k}_c$ with small changes in d_0 is that there may be pinning of the phase of the roll structure by the ramp, as mentioned in the Introduction [20, 21, 24, 27] and as was observed in Taylor-vortex flow with a ramp of the outer cylinder radius. However, DNS of a sample with an aspect ratio considerably smaller than that of ours [12] did not reveal a pinning effect and yielded $\tilde{k}_c = k_c$. Another possibility is that the large-scale and/or mean-flow fields, which couple to the wave director field, are very sensitive to minor differences in alignment of the top and bottom plates relative to each other and/or to gravity; but basically the deviation from k_c and the variation from sample to sample remains an unsolved issue.

As noted before [11], for some of the samples a local wave number outside the stability range of infinitely extended parallel straight rolls is selected at small ε. In those cases dislocations usually formed in the structure. They could move the spatially averaged wave number to the right, i.e. towards or into the stable regime. An example is the lowest point for sample 4 at $\varepsilon = 0.012$. It contained a dislocation similar to those already shown in Fig. 5 of Ref. [11].

Samples 1 to 4 selected patterns that were unstable to skewed-varicose (SV) perturbations for $\varepsilon \gtrsim 0.15$. This instability led to a sustained periodic formation of dislocation pairs. Each pair formation moved the spatially averaged wave number $\langle k_s \rangle$ to smaller values and the local wave number near the sample center back into the stable range. In contrast to samples 1 to 4, the patterns of sample 5 were SV unstable at *all* ε. In that case $\langle k_s \rangle$ oscillated in time with a period that was close to $500 t_v$ and essentially independent of ε. Three examples are shown in Fig. 5. The range of $\langle k_s \rangle$

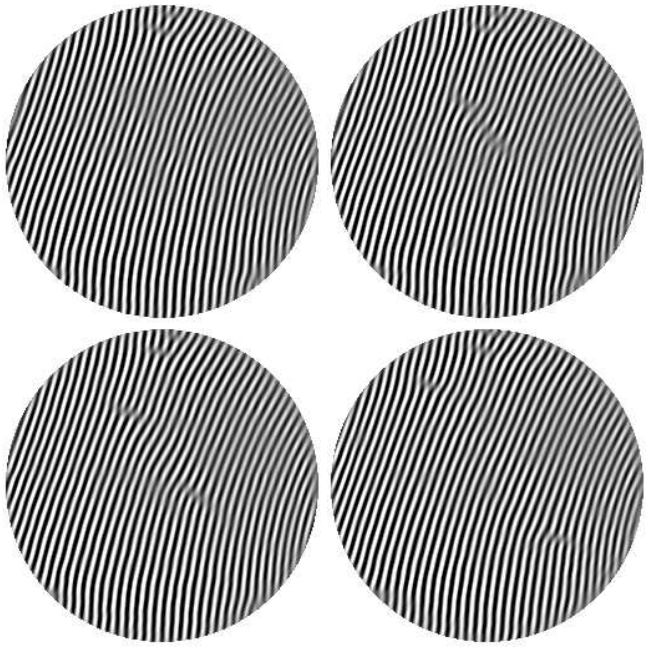

Figure 6. Images for sample 5 and $\varepsilon = 0.054$ for (from left to right and then top to bottom) $t = 993.4$, 961.1, 977.4, and 1031.7. These times correspond to the open circles in the middle panel of Fig. 5. An mpeg movie for this ϵ can be found at Fig6.mpeg. At 30 frames/sec it is running at 450 times real speed. It covers a real-time interval of 128 minutes and shows that the pattern is time dependent.

covered by the oscillations is indicated for each ε by a small horizontal bar in Fig. 4. One can assume that an even larger wave number would have been selected by this sample if the SV instability had not intervened. Examples of patterns from this sample and for $\varepsilon = 0.054$ are shown in Fig. 6. The mean wave numbers of the four images are given as open circles in the middle panel of Fig. 5. The images in Fig. 6 show the formation of a dislocation pair in the interior close to $t = 961$ which at later times separates as the dislocations move to the side wall via a combination of climb and glide. This is seen more clearly in the movie Fig6.mpeg. The ε-independent period of the oscillations and dislocation-pair generation can be understood qualitatively on the basis of a diffusive wave-number adjustment. After a dislocation pair is formed, the local k near the center is in the stable regime, but diffusive phase adjustment re-compresses the rolls and moves the local k back into the SV unstable regime. Such phase diffusion would be approximately ε-independent and would take place on a time scale given by some fraction of the horizontal diffusion time $\tau_h = \Gamma_0^2 \tau_v$.

Another noteworthy feature of Fig. 6 is that the rolls have significantly more curvature in the right part of the images than they have in the left. A comparison with Fig. 2 (the left part of which is also for the same $\varepsilon \simeq 0.05$) shows that this asymmetry was not present for sample 3. It is not possible to tell whether the breaking of the reflection symmetry about a sample diagonal for sample 5 is the cause of the shift of $\langle k \rangle$ to larger values, or whether this shift is a consequence of the repeated

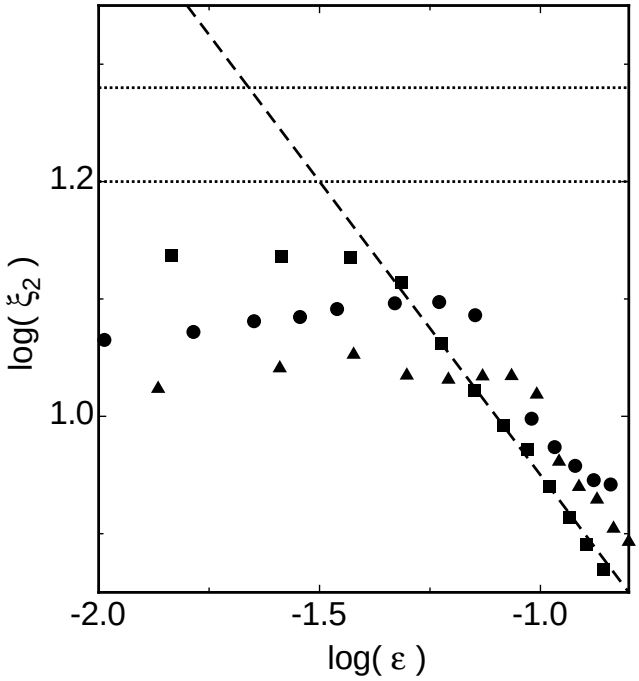

Figure 7. The logarithm of the correlation length ξ_2 as a function of the logarithm of ε. Squares: sample 1. Triangles: sample 2. Circles: sample 3. The dashed line has a slope of 1/2. The horizontal dotted lines indicate the range to be expected if our images consisted of perfect straight rolls.

dislocation generation which is associated with this shift. In any case, one would expect this symmetry breaking to lead to a MF that in turn would couple to the roll structure. Indeed, the asymmetric pattern consists of rolls that are drifting slowly from right to left, as can be see clearly in the movie Fig6.mpeg. This drift was not present for the symmetric pattern of sample 3, as shown in the movie Fig2-right.mpeg.

In Fig. 7 we show the results for the correlation length ξ_2 as defined by Eqs. 5 and 6 on logarithmic scales for samples 1 to 3. The dashed line in the figure has a slope equal to 1/2. One sees that for $\varepsilon \gtrsim 0.05$ ($log(\varepsilon) \gtrsim -1.3$) the data can be described by the powerlaw $\xi_2 = \xi_0 \varepsilon^{-\nu}$ with $\nu = 1/2$. For smaller ε the data for ξ_2 saturate. This saturation could be a consequence of the finite size of the images. The minimum width of the structure factor for a finite image of perfect straight rolls depends on the relationship between the roll wave director and the pixel grid. An analysis of synthetic perfect straight-roll patterns of the same size as the experimental patterns and with the same software yielded values of ξ_2 that depended on the roll orientation. They fell between the two dashed lines in Fig. 7, which is somewhat higher than the experimental values.

4. Summary

In this paper we presented experimental shadowgraph images and their analysis for Rayleigh-Bénard convection of a sample with a radially-ramped section of the cell spacing near the sample periphery. The ramp was introduced to eliminate, reduce, or significantly modify the influence of the side wall on the pattern in the sample interior.

We found nearly-straight roll patterns with mean wave numbers k_s that could be described by $k_s = \tilde{k}_c + k_1\varepsilon$. Surprisingly, $\tilde{k}_c$ was not consistent with the theoretical value $k_c = 3.117$ for RBC in a uniform sample of infinite lateral extent [1] and changed significantly as the sample spacing was modified by small amounts. We do not have an explanation for this behavior, and note that it was not found in direct numerical simulations [12] of the Boussinesq equations of a ramped cell with a smaller aspect ratio. Values obtained for k_1 were close to 0.8 and were consistent with the numerical work of Ref. [12]. As ε increased, the rolls acquired slight curvature and the wave-number distribution became broader. For all samples and at large k, this distribution extended beyond the skewed-varicose instability boundary of the infinite system of straight rolls when ε was sufficiently large (typically greater tham 0.15). For one of our samples, $\tilde{k}_c$ was exceptionally large and the samples were skewed-varicose unstable at *all* $\varepsilon > 0$. In the unstable regime, the samples were time dependent and periodically formed a dislocation pair near their center. The time interval between dislocation-pair formations was about 500 vertical thermal diffucion times and roughly independent of ε. The two dislocations moved, through a combination of climb and glide, radially in opposite directions and disapeared at the sample periphery, thereby making room for the next pair nucleation. When $\tilde{k}_c$ was exceptionally small, dislocations were also observed near onset (but not a slightly larger ε) and were attributed to the Eckhaus instability.[11]

5. Acknowledgment

One of us (GA) is grateful for the hospitality of the Isaac Newton Institute for Mathematical Sciences while writing this paper. This work was supported by the United States National Science Foundation through Grant DMR02-43336.

[1] See, for instance, S. Chandrasekhar, *Hydrodynamic and Hydromagnetic Stability*, (Oxford University Press, London, 1961).
[2] See, for instance, M.C. Cross and P.C. Hohenberg, Rev. Mod. Phys. **65**, 851 (1993).
[3] For a review, see for instance E. Bodenschatz, W. Pesch, and G. Ahlers, Annu. Rev. Fluid Mech. **32**, 709 (2000).
[4] J. Swift and P. C. Hohenberg, Phys. Rev. A **15**, 319 (1977).
[5] P. C. Hohenberg and J. Swift, Phys. Rev. A **46**, 4773 (1992).
[6] J. Oh and G. Ahlers, Phys. Rev. Lett.
[7] A. Schlüter, D. Lortz, and F. Busse, J. Fluid Mech. **23**, 129 (1965).
[8] V. Croquette, Contemp. Phys. **30**, 113 (1989); **30**, 153 (1989).
[9] See, for instance, Y. Hu, R. Ecke, and G. Ahlers, Phys. Rev. E **48**, 4399 (1993); Phys. Rev. Lett. **72**, 2191 (1994); Phys. Rev. E **51**, 3263 (1995).
[10] J. Liu and G. Ahlers, Phys. Rev. Lett. **77**, 3126 (1996).

[11] K.M.S. Bajaj, N. Mukolobwiez, N. Currier, and G. Ahlers, Phys. Rev. Lett. **83**, 5282 (1999).
[12] M.R. Paul, M.C. Cross, and P.F. Fischer, Phys. Rev. E **66**, 046210 (2002).
[13] For a review of the influence of ramps on Rayleigh-Bénard convection, see A. V. Getling, *Rayleigh-Bénard Convection: Structures and Dynamics*, (World-Scientific, Singapore, 1998).
[14] P.M. Eagles, Proc. R. Soc. (London) A **371**, 359 (1980).
[15] L. Kramer, E. Ben-Jacob, H. Brand, and M.C. Cross, Phys. Rev. Lett. **49**, 1891 (1982).
[16] I.C. Walton, Studies Appl. Math. **67**, 199 (1982); Q.J. Mech. Appl. Math. **35**, 33, (1982); J. Fluid Mech. **131**, 455 (1983).
[17] D.S. Cannell, M.A. Dominguez-Lerma, and G. Ahlers, Phys. Rev. Lett. **50**, 1365 (1983)
[18] L. Kramer and H. Riecke, Z. Phys. B **59**, 245 (1985).
[19] J.C. Buell and I. Catton, J. Fluid Mech. **171**, 477 (1986).
[20] M.A. Dominguez-Lerma, D.S. Cannell, and G. Ahlers, Phys. Rev. A **34**, 4956 (1986).
[21] G. Ahlers, D.S. Cannell, M.A. Dominguez-Lerma, and R. Heinrichs, Physica **23D**, 202 (1986).
[22] I. Rehberg, E. Bodenschatz, B. Winkler, and F.H. Busse, Phys. Rev. Lett. **59**, 282 (1987)
[23] H. Riecke and H.G. Paap,Phys. Rev. Lett. **59**, 2570 (1987); H.G. Paap and H. Riecke, Phys. Fluids **A3**, 1519 (1991).
[24] L. Ning, G. Ahlers, and D.S. Cannell, Phys. Rev. Lett. **64**, 1235 (1990).
[25] The LSF differs from the mean flow inducted by roll curvature [26] and roll-amplitude variation [12] in that it is not necessarily associated with net vertical vorticity.
[26] E.D. Siggia ans A. Zippelius, Phys. Rev. Lett. **47**, 835 (1981).
[27] M.C. Cross, Phys. Rev. A **29**, 391 (1984). See also P.M. Eagles, *ibid* **31**, 1955 (1985).
[28] J.R. deBruyn, E. Bodenschatz, S. Morris, S. Trainoff, Y.-C. Hu, D.S. Cannell, and G. Ahlers, Rev. Sci. Instrum. **67**, 2043 (1996).
[29] The properties of various pure gases and of gas mixtures were discussed by J. Liu and G. Ahlers, Phys. Rev. **55**, 6950 (1997).
[30] F. H. Busse, J. Fluid Mech. **30**, 625 (1967). For more recent values of the relevant coefficients, see Ref. [3], Sect. 6.5.
[31] S. Trainoff, Ph. D. Thesis, University of California at Santa Barbara, 1997 (unpublished).
[32] S. Trainoff and D.S. Cannell, Phys. Fluids **14**, 1340 (2002).